Elemental electron energy loss mapping of a precipitate in a multi-component aluminium alloy

Eva A. Mørtsell*[1], Sigurd Wenner[1], Paolo Longo[2], Sigmund J. Andersen[3], Calin D. Marioara[3] and Randi Holmestad[1]

[1]Department of Physics, Norwegian University of Science and Technology (NTNU), 7491 Trondheim, Norway

[2]Gatan Inc., 5794 W Las Positas Blvd, Pleasanton, CA 94588, USA

[3]SINTEF Materials and Chemistry, N-7465 Trondheim, Norway

*Corresponding author. E-mail address: eva.mortsell@ntnu.no

Abstract

The elemental distribution of a precipitate cross section, situated in a lean Al-Mg-Si-Cu-Ag-Ge alloy, has been investigated in detail by electron energy loss spectroscopy (EELS) and aberration corrected high angle annular dark field scanning transmission electron microscopy (HAADF-STEM). A correlative analysis of the EELS data is connected to the results and discussed in detail. The energy loss maps for all relevant elements were recorded simultaneously. The good spatial resolution allows elemental distribution to be evaluated, such as by correlation functions, in addition to being compared with the HAADF image.

The fcc-Al lattice and the hexagonal Si-network within the precipitates were resolved by EELS. The combination of EELS and HAADF-STEM demonstrated that some atomic columns consist of mixed elements, a result that would be very uncertain based on one of the techniques alone. EELS elemental mapping combined with a correlative analysis have great potential for identification and quantification of small amounts of elements at the atomic scale.

Keywords: Al-Mg-Si alloy, EELS, HAADF-STEM, precipitation, Si-network

1 Introduction

The 6xxx series of aluminium alloys are known to gain strength from precipitate phases which are partially coherent with the fcc Al matrix and also based primarily on the main solute elements Mg and Si. The phases grow as needles during heat treatment of the alloy. Their partial coherency means strain-fields are set up in the matrix which will hinder dislocation movement. There are a number of different precipitate phases which can contribute to strength in the 6xxx series, the precipitation sequence in ternary Al-Mg-Si alloy is generally given as [1]:

SSSS → atomic clusters → GP-zones (pre-*β''*) [2] [3] → *β''* [4] [5] → *β'* [6], *U1* [7], *U2* [8], *B'* [9] → *β*, Si (stable)

In the precipitation sequence above, supersaturated solid solution is abbreviated ‘SSSS’ and Guinier-Preston-zones are abbreviated ‘GP-zones’. The crystal structures of the meta-stable phases have mostly been solved by quantitative transmission electron microscopy (TEM) and first principles calculations.

Products of aluminium 6xxx alloys are processed into their final shapes by extrusion or rolling. In the case of extrusion, an important issue is how to keep energy consumption to a minimum. The extrusion process should be efficient while at the same time avoid compromising the final material properties. Pure aluminium is soft with excellent ductility. Any imperfections, like added solutes, will make glides more difficult, thus reducing ductility. While it is clear that extrusion speed can be increased by reducing the amount of solute, strain hardening rate and flow stress will decrease [1], consequently causing a loss in strength in the final product.

In a previous study [10] the overall amount of solute was reduced in a commercial 6060 Al alloy and small quantities of one or a combination of the three elements Cu, Ge and Ag were back-added as an attempt to find the optimal solution to the “strength vs extrudability issue”. In this respect, composition, shape and structure of the precipitates are important parameters which can describe how mechanical properties of the material change. When the alloy contains a higher number of different elements which enter the precipitates, they obviously become increasingly difficult to characterize at the atomic scale and they often become disordered. Disordered precipitates cannot be characterised using one distinct unit cell, since a systematic stacking cannot be detected. In the Al-Mg-Si system, because all precipitates have a similar Si-arrangement, 'disorder' pertains to a precipitate composed of small regions of different precipitate structures, from a subpart of a unit cell up to several cells. The atomic contrast in HAADF-STEM images is due to different proportions of electrons scattered to high angles by different elements. The intensity of atomic columns increases with atomic number (Z) of the elements in the scanned area [11]. HAADF-STEM images are much less affected by objective lens defocus and specimens thickness than high resolution TEM images. Since the alloy in this work has a large range of (Z, HAADF-STEM is particularly useful to study the precipitates.

Since elements like Mg, Al and Si are very close neighbours in the periodic table, and the observed atomic columns might be expected to consist of more than one element, HAADF-STEM images of the precipitates may be difficult to interpret correctly. EELS spectrum imaging can help to overcome this problem since each element adds a unique fingerprint to a spectrum through its core loss edge at a specific energy.

Previously, atomic scale EELS mapping of Cu and Ag in precipitates in 6xxx Al alloys has been executed successfully [12], however, as far as we can see, there have been no reported studies where Mg, Si or Ge have been mapped in such precipitates. In this work we demonstrate how this technique represents a significant advance regarding analysis of precipitates in an Al-Mg-Si-Cu-Ag-Ge alloy.

2 Experimental

The composition of the investigated alloy is presented in Table 1, as measured by inductively coupled plasma optical emission spectroscopy.

Table 1 Quantified alloy composition and effective solute (S_{eff})

	Si[a]	Ge	Mg	Cu	Ag	Fe	Mn	S_{eff} [b]
wt%	0.35	0.03	0.30	0.03	0.03	0.20	0.03	0.69
at%	0.34	0.011	0.33	0.013	0.008	0.10	0.015	0.65

[a] Effective Si amount available for precipitation (Si*) is 0.05 wt % less than tabulated value [13]. [b] Total effective solute S_{eff} = Mg+Si*+Ge+Cu+Ag.

The alloys were cast as cylindrical billets of 4 kg. The billets were homogenized at 575 °C for 3 hours and cooled to room temperature (RT) in air. The billets were extruded as round profiles with a diameter of 2 cm, and water quenched to room temperature within 5 seconds.

Samples (1 cm thick disks of diameter 2 cm) were cut from the extruded profiles perpendicular to the extrusion direction. The samples were solution heat treated (SHT) in an air circulating furnace for 5 minutes after reaching 535 °C, and immediately water quenched to RT. The samples were held at room temperature for 4 hours and then subjected to artificial ageing (AA) in an air circulating furnace keeping a final temperature of 195 °C for 4 hours.

TEM specimens were prepared using a TenuPol-5 electropolishing unit from Struers. The electrolyte consisted of one part HNO_3 and two parts methanol, and was kept at temperatures between -25 °C and -30 °C by adding liquid nitrogen. The specimens were finally cold-stage ion polished in a Gatan PIPS at voltages below 3 keV. The thickness of the specimen is expected to be around 30 nm in the investigated area.

A complete description of the heat treatment can be found in previously published work [10], where also hardness curves and TEM precipitate statistics from the current material can be found. To minimize contamination on the specimen surfaces, plasma cleaning was performed for 7 minutes in O_2/Ar plasma using a Fischione plasma cleaner model 1020.

The high angle annular dark field scanning TEM (HAADF-STEM) and EELS results were obtained in a double spherical aberration (Cs) corrected JEOL ARM200F with a cold field emission gun (FEG). The microscope was equipped with a Quantum Gatan image filter (GIF). The operation voltage was 200 kV and the probe size was about 0.08 nm. The dispersion was 1.0 eV/channel. A Gatan annular dark field detector was used, where the inner and outer detector angles read 67- and 155 mrad, respectively. With a dispersion of 1 eV, the GIF gives a 2000 eV field of view.

EEL spectra were acquired in the energy loss range 280-1900 eV. This energy loss range includes the edges Ag-$M_{4,5}$ at 367 eV, Cu-$L_{2,3}$ at 931 eV, Ge-L1, 2 and 3 at 1217, Mg-K at 1305 eV, Al-K at 1560 eV and Si-K at 1839 eV. The elemental maps were created using Gatan's software package Digital Micrograph. The manual integration of EELS edges were performed after power-law background subtraction.

Auto correlation was applied to each of the EELS maps to determine their self-similarities. This was done in Digital Micrograph by first performing a Fourier transform of the map. The resulting image was multiplied by its complex conjugate, and finally an inverse Fourier transform was calculated based on the preceding image [14]. Also, cross correlations were performed in order to check the similarities between two EELS maps. Here, a Fourier transform was performed on each of the two maps. The Fourier transform of the first map was then multiplied by the complex conjugate of the Fourier transform of the second map. Finally, the inverse Fourier transform of the resulting image was calculated [14]. The maximum area from which it was possible to perform auto- and cross correlations was used in all cases, except for the Si auto correlation of the β''-like area in Fig. 3 (b).

3 Results

Fig. 1 shows the raw HAADF-STEM image of the investigated precipitate cross section before the EELS scan. The area scanned by EELS is indicated in the image.

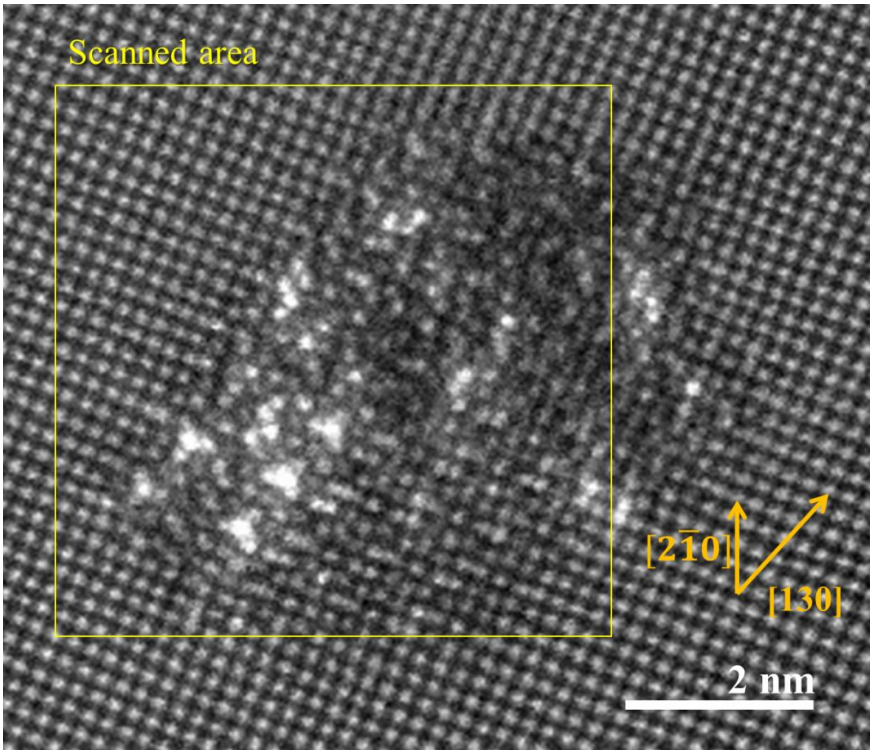

Fig. 1 HAADF-STEM image before the EELS scan of a precipitate cross section. The yellow square indicates the boundary of the area scanned for EELS mapping, the area is equivalent to the mapped regions presented in Figs. 2 and 5.

The elemental EELS maps are presented in Fig. 2, showing that Si, Mg, Al and Ag were detected within the precipitate cross section. Several intensity peaks in Fig. 2 (a) – (d) correspond well with single atomic column positions in Fig. 1. However, regarding the Ge and Cu maps, the signal to noise ratio was too low to get any information. The weak signal was a consequence of reducing the dose of the electron beam in order to preserve the sample from beam damage, also, the concentration of Ge and Cu in this particular precipitate seems

to have been low. The Ge and Cu maps are still presented for comparison in Fig. 2 (e) and (f), respectively.

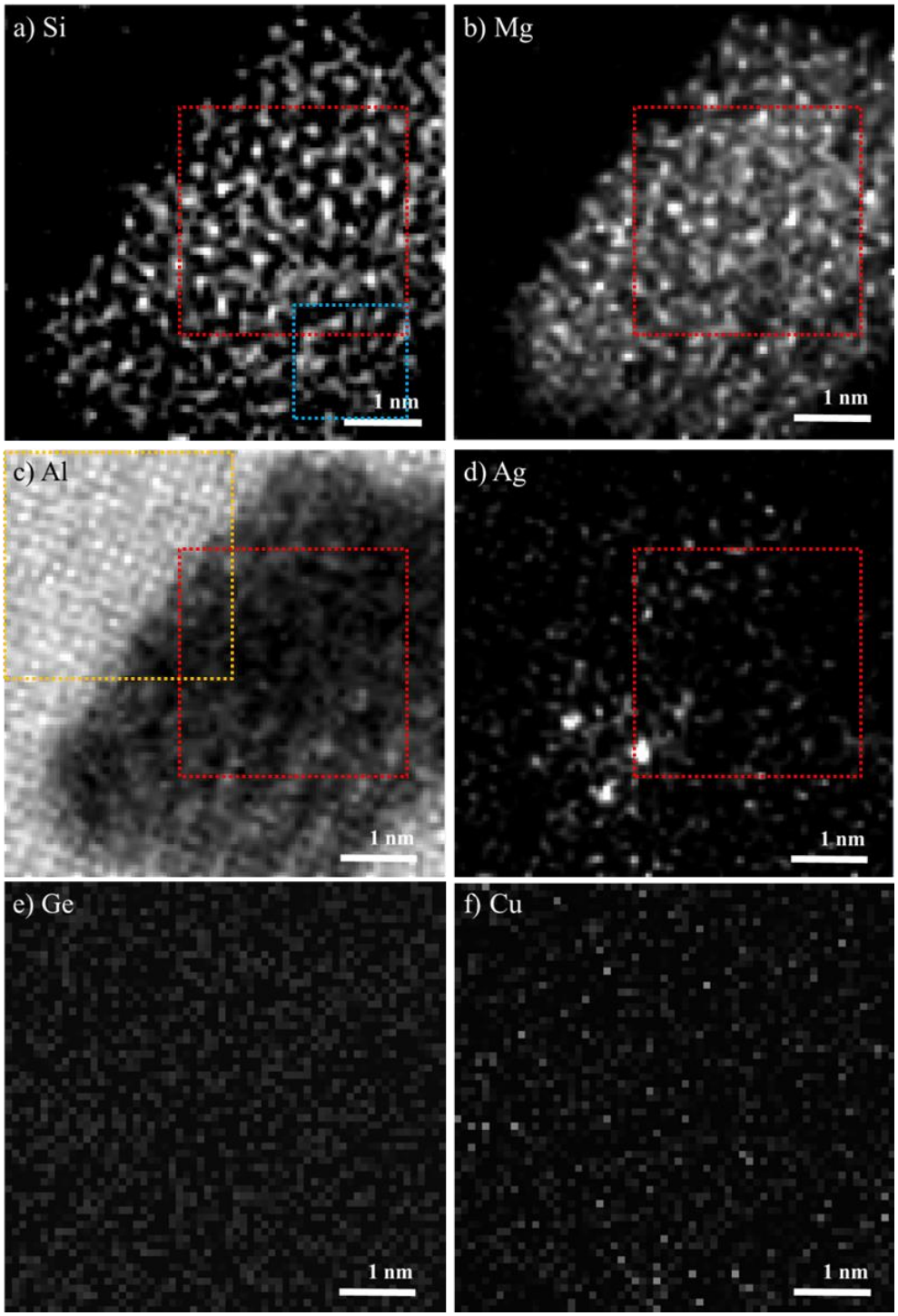

Fig. 2 EELS elemental maps, the red squares indicate areas chosen for auto correlations in Fig. 3 and cross correlations in Fig. 4 **(a)** Si-K edge, the blue square: auto correlation area of *β''* – like features observed in the HAADF-STEM image in Fig. 1, **(b)** Mg-K edge, **(c)** Al-K edge, yellow square: auto-correlation of Al, **(d)** Ag-M edge, **(e)** Ge-L edge and **(f)** Cu-L edge.

To find information on the periodicities in each EELS map, auto correlation maps were constructed for the four elements Si, Mg, Al and Ag. These are given in Fig. 3. The auto correlation map of Al is based on the Al matrix, the area is marked by a yellow square in Fig. 2 (c). The residual maps are based on equivalent areas from the precipitate cross section, see Fig. 2. The comparison of similarity between the EELS maps of different elements are given by cross correlations in Fig. 4. Cross correlation is based on the same areas from the precipitate cross section when comparing two elements.

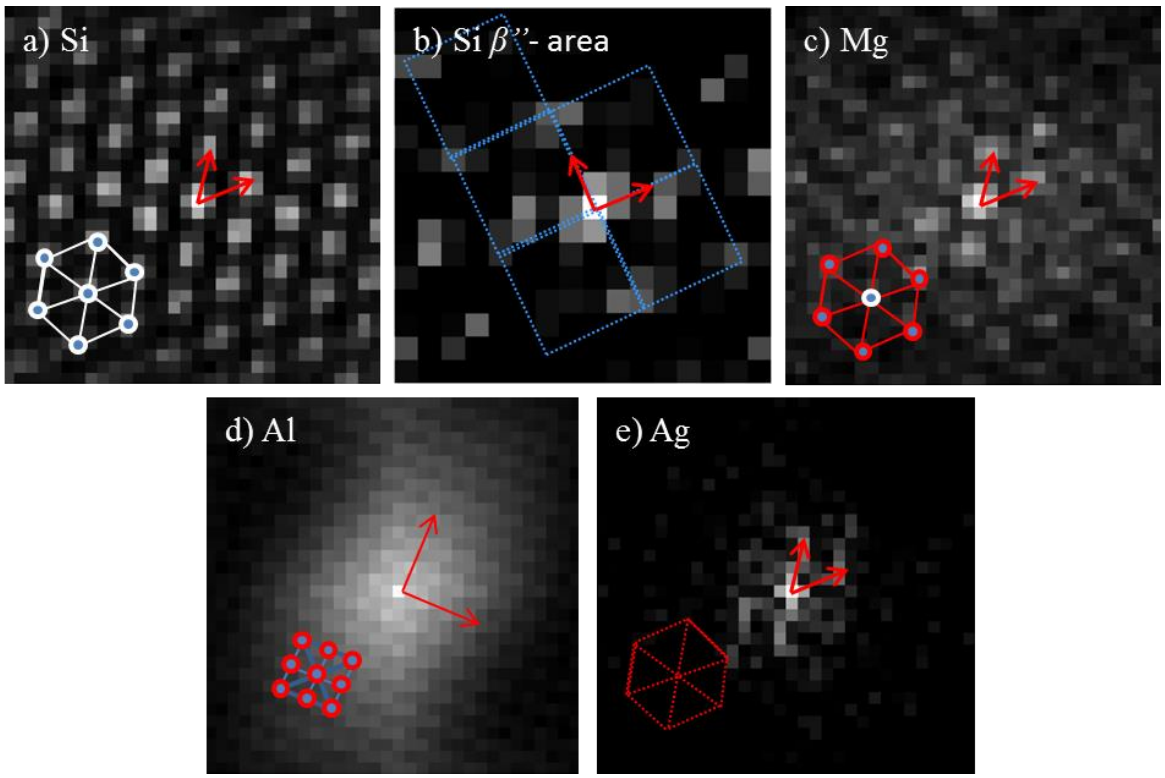

Fig. 3 Auto-correlation functions based on the EELS maps of the respective elements: **(a)** the Si-K edge from the area marked by a red square in Fig. 2, **(b)** the Si-K edge from the area marked by a blue square in Fig. 2. A square pattern appearing in addition the hexagonal pattern in (a) is highlighted with blue lines. The pattern appears larger because of the smaller selected area **(c)** the Mg-K edge from the area marked by a red square in Fig. 2 (b), **(d)** the Al-K edge from the area marked by the yellow square in Fig. 2 (c) and **(e)** the Ag-M edge from the area marked by the red square in Fig. 2 (d). The filled circles attached with solid lines indicate the pattern of intensity peaks in each image. The arrows illustrate vectors between intensity peaks in the auto correlation, describing areas of self-similarity in each image.

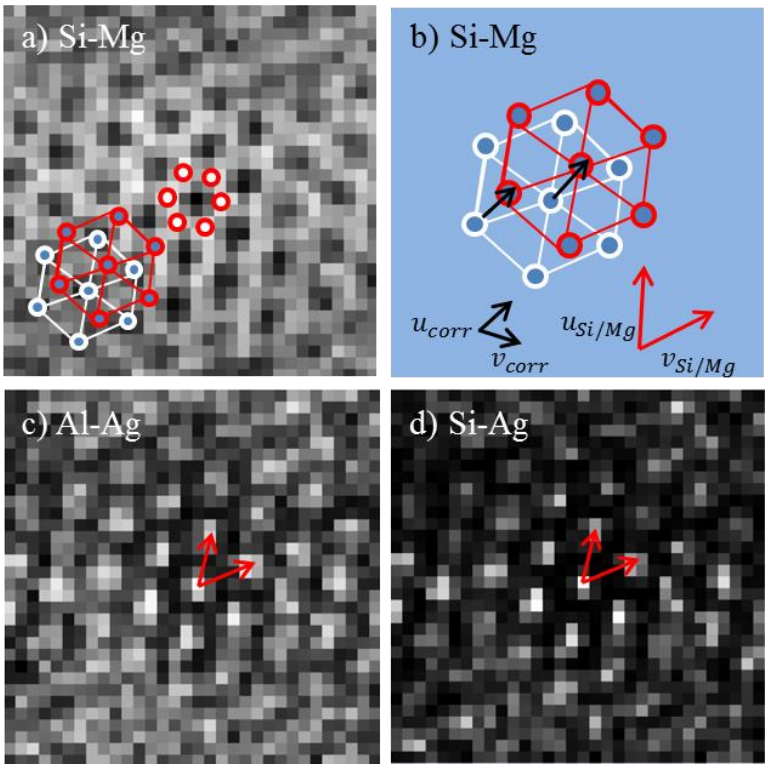

Fig. 4 Cross correlation functions based on the EELS maps: **(a)** Si-K edge and Mg-K edge. The red circles filled with white indicate the intensity peaks. The two hexagons illustrate the hexagonal patterns from the auto correlation of Si and Mg given in Fig.3, **(b)** enlarged view of the hexagonal pattern in (a) where black arrows, marked u_{corr} and v_{corr}, illustrate the displacement of the Si intensity peaks needed to coincide with the Mg intensity peaks and vice versa. The vectors $u_{Si/Mg}$ and $v_{Si/Mg}$ in red from the auto-correlation of Si and Mg in Fig. 3 are given for comparison, **(c)** Al-K edge and Ag-M edge and **(d)** Si-K edge and Ag-M edge. Arrows indicate the displacement needed for the two signals to coincide.

4 Discussion

The HAADF-STEM image in Fig. 1 resolves the fcc Al lattice and the atomic column arrangement of the precipitate needle cross section to be discussed. From this image it is clear that one or more element with a relatively high Z is present, particularly in the lower left region of the needle cross section, which exhibits a triangular arrangement of atomic columns. The lower right part of Fig. 1 seems to contain fragments resembling the eye-like features of the β'' phase, in which Si columns arrange in squares [4]. The β'' area is less distinct compared to the rest, suggesting that the needle does not extend all the way through the sample; consequently it should be partly covered by the Al matrix here. The remainder of the precipitate cross section seems partly disordered with fragmented triangular symmetry.

The EELS maps reveal more information about the atomic column arrangement in this complex precipitate cross section. Close investigation of the Si map in Fig. 2 (a) reveals a set of distinct intensity peaks forming a hexagonal pattern across a majority of the precipitate cross section. Such hexagonal Si-networks have been discussed in several previous publications [15], but it has not yet, to the best of our knowledge, been detected by elemental

specific, atomic resolution, characterization techniques. The arrangement of Si-columns should however be square in the β'' – region. There are square features in this region from Fig. 2 (a), but they are not evident by eye, this is to be discussed further below.

The auto correlation of the Si map in Fig. 3 (a) demonstrates the self-similarity of the Si arrangement. The pattern of intensity peaks is indicated with solid circles and solid lines. The arrows in Fig. 3 show, in simple words, how far the Si signal needs to be moved in order to coincide with itself. A hexagonal pattern clearly stands out, telling us that Si must be ordered in columns which form a hexagonal pattern in the precipitate cross section. The distance between the Si columns is approximately 4 Å when comparing the EELS map and the HAADF-STEM image. It can be concluded from this that we are in fact dealing with the above mentioned Si-network [15]. The square pattern corresponds exactly to the ordering and direction of Si columns in the β''-eyes. It should be noted that the intensity peaks in Figs. 3 and 4 are more prominent along the x-direction than in the y-direction. This is because the fast scan direction is along the x-direction, causing the y-direction to be noisier.

While an overall arrangement of Mg columns from the EELS map in Fig. 2 (b) is not obvious, quite a few intensity peaks stand out. The immediate impression from the Mg map is that Mg is not as bound to particular sites as Si, consequently the intensity is more diffuse across the map. It is however clear that Mg is residing within the precipitate cross section, and there is no significant signal from the Mg-K edge in the Al matrix. The auto correlation of Mg given in Fig. 3 (c) gives us some interesting additional information. It seems that sites occupied by Mg exhibit an overall hexagonal ordering within the precipitate cross section. Although more diffuse than for Si, the hexagonal pattern based on Mg in Fig. 3 (c) cannot be mistaken.

When the EELS map from the Al-K edge was extracted, the Al-lattice surrounding the precipitate stands out, see Fig. 2 (c). Because of the much lower density and non-continuous periodicity of Al columns inside the precipitate the signal is harder to make out here. The lower right part of the precipitate cross section, seemingly being partly overlapped by Al from Fig. 1, does indeed show an increased signal in the Al EELS map. There is also a diffuse Al signal, with some atomic columns standing out, from within the cross section. The auto correlation of Al in Fig 3 (d) shows a square pattern analogous to that of the Al lattice. It can be concluded that atomically resolved EELS picks up the periodicity of the Al lattice.

In Fig. 2 (d) it becomes evident that the high intensity columns located at the lower left of the precipitate cross section must be occupied by silver. Some signal from the Ag-M edge is also emanating from other parts of the precipitate, including a diffuse intensity surrounding the obvious Ag columns.

The hexagonal Si-network is known to be replaced by a similar Ge-network when Ge is added to the alloy [17]. The Ge-L edge could not be detected by EELS for this particular precipitate, see Fig. 2 (e). One might speculate that the Si columns from the EELS map have a very small Ge occupancy based on findings in previous publications [17], however that the

signal to noise ratio was too low to detect Ge in this case. The most probable conclusion is however that this particular precipitate does not accommodate any Ge.

From Fig. 2 (f) it might be argued that a very faint Cu signal is present, although the signal is the same everywhere in the map. In Fig. 1 some known configurations usually containing Cu can be singled out. It is possible that the central atomic columns in the triangular configuration typically consisting of Cu can be replaced by other elements, since the signal is very low here [16].

Although the auto correlations of Si and Mg (Fig. 3 (a) and (c)) may appear similar, cross correlating the two, see Fig. 4 (a), reveals that the two are not located at the same sites in the precipitate cross section. In fact, from the cross correlated area of the precipitate cross section it can be seen that Si and Mg are never co-located at any point. This is also illustrated in Fig.4 (b) with vectors showing how the two signals must move relative to each other in order to overlap. This suggests a triangular arrangement of Mg columns surrounding each Si-network column, a model already discussed thoroughly by Ehlers et al. [18]. The model suggests that a small set of local geometries can fully explain all precipitate needle cross section structures from the 6xxx alloy series. From these results, it should be possible to decompose the precipitate cross section from Fig. 1 into geometrical units based on the location of Si-network columns found in Fig. 2 (a).

The cross correlation of Al and Ag in Fig. 4 (c) indicates that the two elements occupy some of the same atomic columns, where the "co-occupation" forms a hexagonal pattern. Since Ag is found inside the cross section, we expect to see a tendency of hexagonal Ag ordering, as it often occupies Si column positions [19]. Since Ag exhibits a much stronger signal than Al, and it is reasonable to believe we have more Ag inside the needle precipitate than in the matrix, the cross correlation between Al and Ag from within the particle should be hexagonal.

The cross correlation between Si and Ag in Fig. 4 (d) shows a very good fit between Si and Ag in the precipitate cross section. From these results it is evident that Si and Ag must occupy a significant amount of the same sites, also in areas where the signal from Ag is too low to be detected by eye.

Based on known local symmetries, the Z-contrast information of individual atomic columns and knowledge of precipitate structures in Al-Mg-Si alloys with other solute additions, we can compare the EELS maps and HAADF-STEM image and reveal the most probable atomic overlay of the columns in this precipitate cross section. As we have identified Ag to be the most likely "high Z element" present in the precipitate in Fig. 2, we will assume Si to be the element exhibiting the second highest intensity in Fig. 1. The visualization of the hexagonal Si network is shown in Fig. 5 (a). Earlier work shows that the triangular symmetry marked by green triangles connecting triplets of Si atoms Fig. 5 (a) most likely are Cu sites [16]. The very low Cu intensity suggests that this configuration perhaps exchanges Cu with Ag. The centres of these triangles have high intensity peaks in the HAADF-STEM image, but are not

shown explicitly in Fig. 5. The square configuration of the Si columns in the β'' region of the precipitate are marked with green squares in Fig. 5 (a).

The intensity peaks from the Mg EELS map correspond to a significant amount of columns in the HAADF-STEM image. The atomic columns from EELS which fit well with the local geometry approach described in [18], are indicated with green symbols in Fig. 5 (b). The Mg EELS map is, as mentioned earlier, more diffuse than the Si and Ag maps, hence low intensity areas not corresponding well with local geometries are not marked in this figure. However, some additional known Mg configurations can be identified. These particular configurations are pointed out by triangles in Fig. 5 (b) correlating with those in Fig. 5 (a), indicating Mg together with Si forming the triangular symmetry associated with the Cu configuration. Also, the larger triangles of black double lines indicate the column distribution of Mg which is found to exist in the β'_{Ag} phase [19]. Finally, the square arrangement of Mg columns in the equivalent positions in the β'' phase is recognised. These Mg columns are marked by squares (both complete and incomplete) in Fig. 5 (b).

From Fig. 1 and Fig 2 (d) it is possible to deduce that that all the obvious Ag atomic columns in the precipitate are placed in a local β'_{Ag} configuration [19], see also the final model in Fig. 6. In this structure the three nearest atomic columns to the central Ag column are Al, as identified by EELS, see the connected black lined triangles in Fig. 5 (c). These columns do however exhibit high Z-contrast in the HAADF-STEM image, which may indicate they are mixed Ag/Al-columns or that some of the intensity from the central Ag columns spills into nearby columns. It can be speculated that the hexagonal pattern in Fig. 4 (c) is partly a consequence of Ag diffusing from its preferred sites and into nearby Al columns [12].

Based on Z-contrast and local symmetry in the HAADF-STEM image, the sites marked by a red X in Fig. 5 (a) should be occupied by Ag as in the β'_{Ag} phase, and signal from the Ag-M edge is, as expected, found to originate from these sites, as pointed out with stars in Fig. 5 (d). However, the Si map in Fig. 5 (a) also shows a significant intensity at the same sites, meaning that these columns must be mixed Ag/Si.

One column has been marked with a red '+' in Fig. 5 (a). This column has a very high Z-contrast in the HAADF-STEM image and cannot only consist of Si. Consequently, the column should be mixed with one or more of the three heavier elements Ag, Cu or Ge. Taking into account the low EELS signal from Cu and Ge and that the nearby columns have a relatively high intensity in the HAADF-STEM image, it is likely that the columns are Ag enriched or subjected to intensity spread. It has been observed by Wenner et al. that Ag-rich areas do not overlap with Cu atomic columns [12]. Moreover, during the scan, silver might have diffused into nearby columns, or the intensity spread could be due to delocalization of the M-edges of silver, which can result in an apparent intensity spread to surrounding columns [11].

An interesting site from the Mg map is marked by a yellow X in Fig. 5 (b) and (c), here a weak Mg signal was detected, making it possible to consider this as a mixed Al/Mg column. According to both the C-plate and the Q-phase models [20], this site should be only Al,

however, from quantitative nano-beam diffraction data of the Q' phase [21] this site should indeed be mixed Al and Mg.

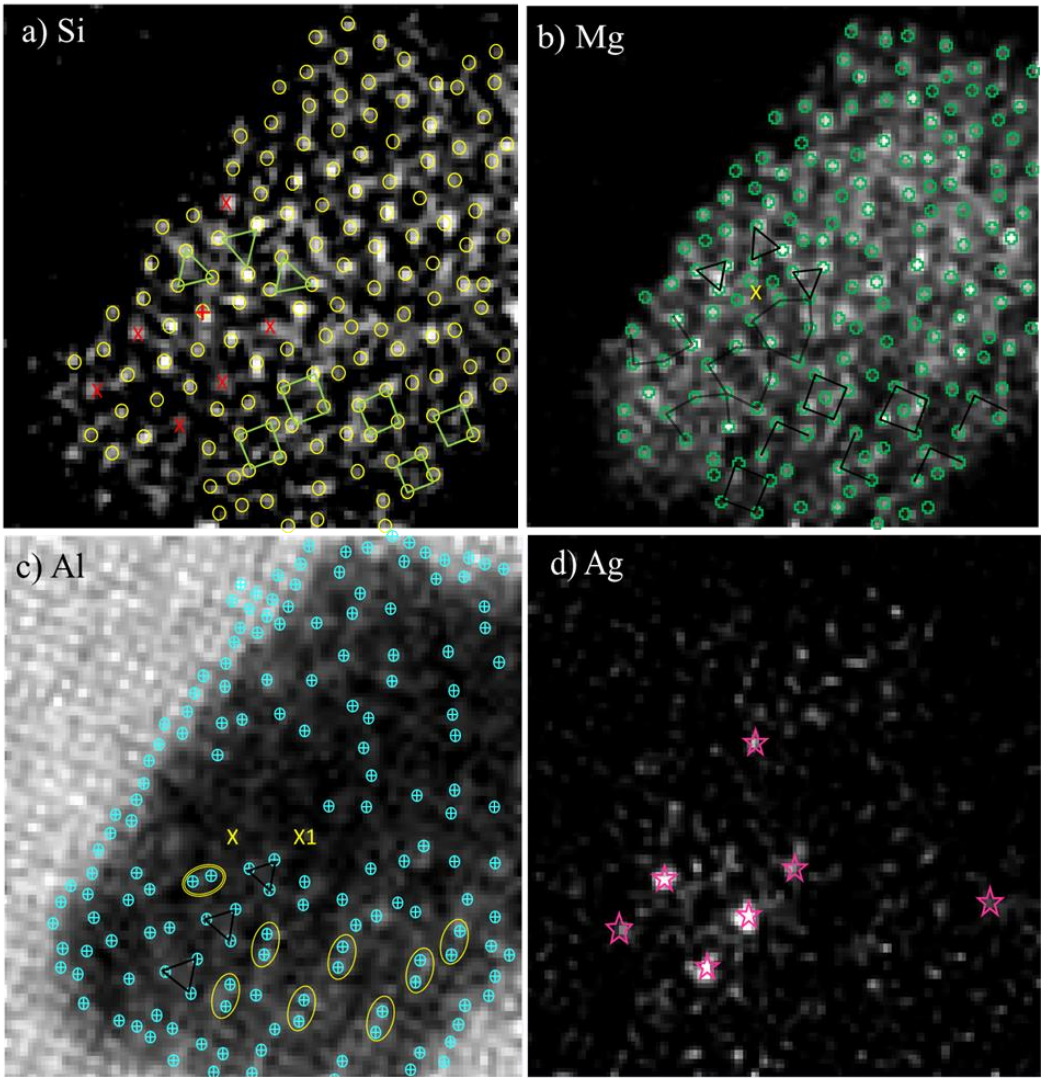

Fig. 5 EELS elemental maps of a) The Si-K edge, b) the Mg-K edge, c) the Al-K edge and (d) the Ag-M edge with overlays of specific details in the atomic columns. See text for detailed explanations.

Table 2: Symbolic representation of elements in Figs. 5 and 6.

Elements / Height	Al	Si	Mg	Cu	Ag
z = 0.000 nm	⊕	○	⌬	◎	☆
z = 0.203 nm	●	●	●	◉	★

The X1 site in Fig. 5 (c) marks a column which according to the atomic overlay is expected to be a Si column. The EELS map of Si does certainly indicate some Si at this site, however, the Al signal from the Al map is even stronger. Since the Z-contrast of this column is relatively low, it is likely that we are dealing with a mixed Al/Si column. Determining this

column to be mixed Al and Si would be impossible based on the HAADF-STEM image alone.

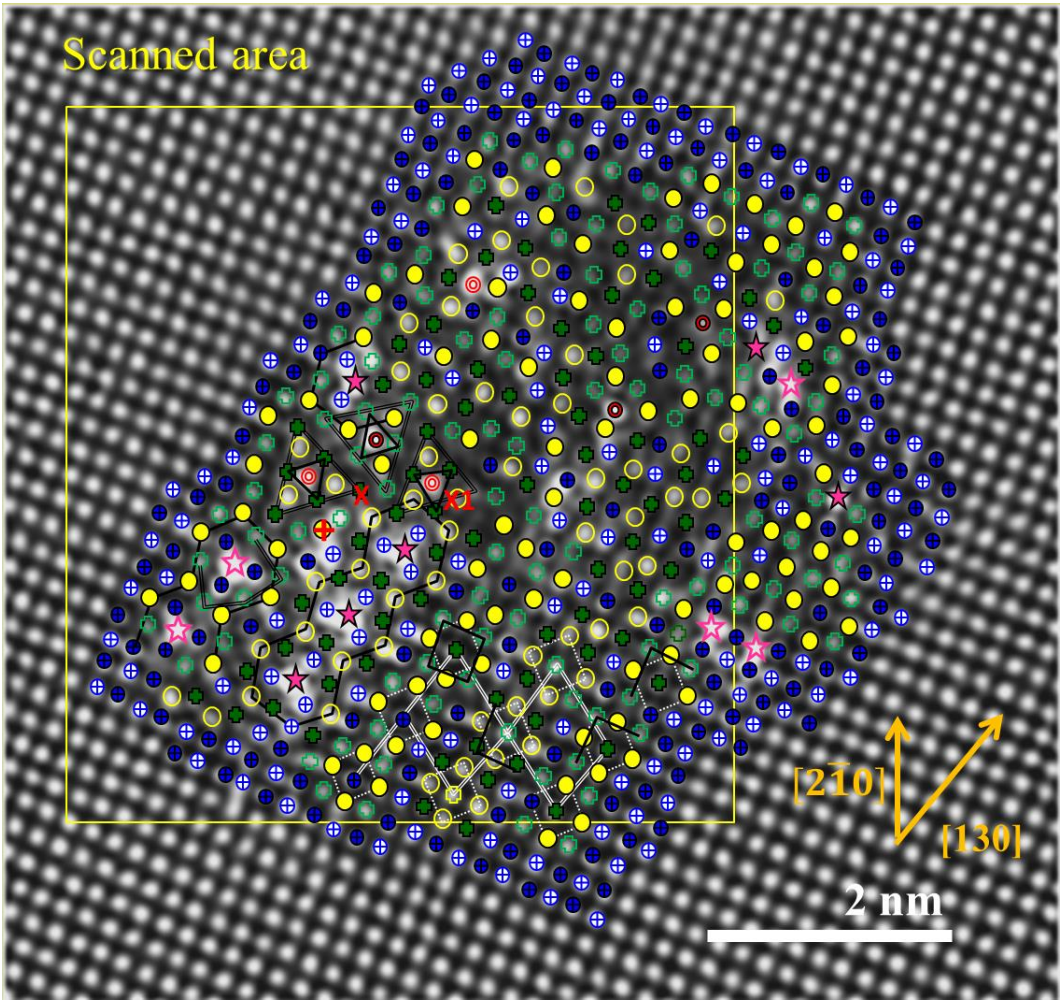

Fig. 6 Suggested atomic overlay based on the HAADF-STEM image from Fig. 1, EELS maps in Fig. 2, local geometries and the results in Figs. 3 and 4. For atomic column designation and heights, see legend in Table 2. The yellow square delimits the area of the EELS mapping, which is also equivalent to the regions presented in Figs. 2 and 5. The overlay is also based on knowledge of various precipitate structures and their internal units and symmetries (such as the square units of β'' [4]or the arrangement around Ag columns in β' [6]) together with the identification of the Si-network [15]. The known heights of the surrounding Al matrix and the necessary connections between the different structural units enable a bootstrapping of the heights over the whole cross-section.

Based on the initial HAADF-STEM image in Fig. 1, the EELS maps in Fig. 2, correlation analysis, local geometry considerations and knowledge of previously well-known precipitate phases, we propose the model in Fig. 6 as the most probable distribution of atomic columns within the precipitate cross section. A few additional comments should be given based on the insight obtained from this analysis. By comparing Fig. 6 to Fig. 5 (c) we see that the yellow ovals show pairs of Al columns which correlate to the Mg and Si pattern in Fig. 5 (a) and (b), showing they are the Si3/Al sites of two neighbour molecules in *β''*. The yellow ovals in Fig.

5 (c) indicate columns which are expected to be Al according to local geometry. Even though an Al signal is detected by EELS, the HAADF-STEM image shows high Z-contrast at the very same sites. Based on these findings, the yellow ovals are interpreted as columns of Al mixed with Ag.

Elemental mapping by EELS has a great potential for precipitate characterization on the atomic scale. By applying auto correlation and cross correlation techniques it is possible to extract global information from the elemental maps not apparent by eye. Several results from the HAADF-STEM and EELS studies could not have been attained without combining these techniques. In particular, columns in the precipitate cross section containing more than one element would be impossible to determine unequivocally.

5 Conclusions

A cross section belonging to a precipitate needle in a Al-Mg-Si-Cu-Ag-Ge 6xxx Al alloy has been investigated by HAADF-STEM, EELS and a correlative analysis of the EELS results. It has been shown that EELS elemental mapping is possible at the atomic scale for these types of precipitates and that the technique can be used to identify elements present in the precipitates. In particular, EELS could resolve the fcc lattice in the Al matrix and verify the existence of the hexagonal Si-network in 6xxx alloy precipitates. The correlative analysis based on the EELS results shows a global hexagonal arrangement of Si, Mg and Ag inside the precipitate, where Mg and Si do not coincide at any point. Specific sites where atomic columns consist of a mix of elements have been determined when combining EELS and HAADF-STEM images. Determination of mixed columns would be impossible in many cases when relying on only one of the techniques.

Acknowledgements

This work has been supported through the BIA RolEx project, no. 219371 by Hydro Aluminium and the Research Council of Norway. The TEM/STEM and EELS work was carried out on the NORTEM JEOL ARM200F, TEM Gemini Centre, Norwegian University of Science and Technology (NTNU), Norway.

Bibliography

[1] C. D. Marioara, H. Nordmark, S. J. Andersen and R. Holmestad, *J. Mater. Sci.,* vol. 41, pp. 471 - 478, 2006.

[2] G. A. Edwards, K. Stiller, G. L. Dunlop and M. J. Couper, *Acta Mater.,* vol. 46, pp. 3893 - 3904, 1998.

[3] C. D. Marioara, S. J. Andersen, J. Jansen and H. W. Zandbergen, *Acta Mater.,* vol. 49, pp. 321 - 328, 2001.

[4] S. J. Andersen, H. W. Zandbergen, J. Jansen, C. Træholt, U. Tundal and O. Reiso, *Acta Mater.*, vol. 46, pp. 3283 - 3298, 1998.

[5] H. S. Hasting, A. G. Frøseth, S. J. Andersen, R. Vissers, J. C. Walmsley, C. D. Marioara, F. Danoix, W. Lefebvre and R. Holmestad, *J. Appl. Phys.*, vol. 106, 2009.

[6] R. Vissers, M. A. v. Huis, J. Jansen and C. D. M. S. J. A. H. W. Zandbergen, *Acta Mater.* , vol. 55, pp. 3815 - 3823, 2007.

[7] S. J. Andersen, C. D. Marioara, R. Vissers, A. Frøseth and H. W. Zandbergen, *Mater. Sci. Eng. A*, vol. 444, pp. 157 - 169, 2007.

[8] S. J. Andersen, C. D. Marioara, A. Frøseth, R. Vissers and H. W. Zandbergen, *Mater. Sci. Eng. A*, vol. 390, pp. 127 - 138, 2005.

[9] R. Vissers, C. D. Marioara, S. J. Andersen and R. Holmestad, *Aluminium Alloys*, vol. 2, pp. 1263 - 1269, 2008.

[10] E. A. Mørtsell, C. D. Marioara, S. J. Andersen, J. Røyset, O. Reiso and R. Holmestad, *Met. Trans. A*, 2015.

[11] M. D. Rossel, Q. M. Ramasse, S. D. Findlay, F. Rechberger, R. Erni and M. Niederberger, *ASC Nano*, vol. 6, pp. 7077 - 7083, 2012.

[12] S. Wenner, C. D. Marioara, Q. M. Ramasse, D. M. Kepaptsoglou, F. S. Hage and R. Holmestad, *Scripta Mat.*, vol. 74, pp. 92 - 95, 2014.

[13] U. Tundal, O.Reiso, E. Hoff, R. Dickson and C. Devadas, in *Proc. 10th International Aluminum Extrusion Technology Seminar*, Miami, 2012.

[14] G. Inc., "Fourier processing," in *Digital Micrograph 3.4 User's Guide* , Pleasanton, gatan, 1999, pp. 8-1 - 8-4.

[15] S. J. Andersen, C. D. Marioara, R. Vissers, A. L. Frøseth and P. Derlet, in *Proc. 13th Eur. Mocr. Congress (EMC) 2*, 2004.

[16] T. Saito, C. D. Marioara, S. J. Andersen, W. Lefebvre and R. Holmestad, *Philosophical Magazine*, vol. 94, no. 5, pp. 520 - 531, 2015.

[17] C. D. Marioara, J. Nakamura, K. Matsuda, S. J. Andersen, R. Holmestad, T. Sato, T. Kawabata and S. Ikeno, *Phil. Mag.*, vol. 92, pp. 1149 - 1158, 2012.

[18] J. Bobynko, I. MacLaren and A. J. Craven, *Ultramicroscopy*, vol. 149, pp. 9-20, 2015.

[19] M. Torsæter, F. J. H. Ehlers, C. D. Marioara, S. J. Andersen and R. Holmestad, *Philosophical Magazine*, vol. 92, no. 31, pp. 3833 - 3856, 2012.

[20] M. Torsæter, R. Vissers, C. D. Marioara, S. J. Andersen and R. Holmestad, *Proceedings of ICAA11*, vol. 2, p. 1338, 22 - 26 September 2008.

[21] R. Bjørge, C. D. Marioara, S. J. Andersen and R. Holmestad, *Metal. Mater. Trans. A*, vol. 41, p. 1907, 2010.

[22] D. McLeod, Mechanical Properties of Metals, New York: John Wiley & Sons, 1962, p. 162.

[23] T. Yamazaki, M. Kawasaki, K. Watanabe, I. Hashimoto and M. Shiojiri, *Ultramicroscopy*, vol. 92, p. 181, 2002.

[24] P. D. Nellist and S. J. Pennycook, *Ultramicroscopy*, vol. 78, p. 111, 1999.

[25] G. P. M. Leyson, L. G. Hector and W. A. Curtin, *Acta Mat.*, vol. 60, pp. 3873 - 3884, 2012.

[26] C. Wolverton, *Acta Mater.* , vol. 55, pp. 5867 - 5872, 2007.

[27] S. J. Andersen, C. D. Marioara, R. Vissers, A. Frøseth and H. W. Zandbergen, *Mater. Sci. Eng. A*, vol. 444, p. 157, 2007.

[28] C. D. Marioara, S. J. Andersen, T. N. Stene, H. Hasting, J. Walmsley, A. T. J. V. Helvoort and R. Holmestad, *Philosophical Magazine*, vol. 87, p. 3385, 2007.

[29] K. Matsuda, Y. Uetani, T. Sato and S. Ikeno, *Metall. Mater. Trans. A*, vol. 32, p. 1293, 2001.

[30] C. Cayron, L. Sagalowicz, O. Beffort and P. A. Buffat, *Philos. Mag. A*, vol. 79, p. 2833, 1999.

[31] F. J. H. Ehlers, S. Wenner, S. J. Andersen, C. D. Marioara, W. Lefebvre, C. B. Boothroyd and R. Holmestad, *J Mater Sci*, vol. 49, pp. 6413 - 6426, 2014.